

Variations of the Galactic Cosmic Rays in the Recent Solar Cycles 23 & 24

Brijesh Dwivedi^{1*}, Dr. Achyut Pandey²

¹ Phd Scholar, APSU Rewa

Email: bwivedi233@gmail.com

² HOD, Physics and Head of Computer Science, TRS College, Rewa

Email: achyut.pandey9@gmail.com

Abstract - In this study, we examine During solar cycles 23 and 24, the Galactic cosmic-ray (GCR) oscillations were explored using data from NASA's Advanced Composition Explorer/Cosmic Ray Isotope Spectrometer instrument and ground-based neutron monitors (NMs). The findings show that at the solar minimum in 2019-2020, the maximum GCR intensities of heavy nuclei ($5 < Z < 28$, 50500 MeV nuc⁻¹) at 1 au exceed previous records by about 25% and 6%, respectively, and reach their highest values throughout the space age. Peak NM count rates, on the other hand, are lower than in late 2009. The difference in NM count rates and GCR intensity is currently unaccounted for. Furthermore, we discover that the GCR modulation environment P24/25 of the solar minimum varies from previous solar minima in key ways: a comparatively small amount of sunspots There is very little tilt in the heliospheric current sheet, rare coronal mass ejections, a weak interplanetary magnetic field, and turbulence. These modifications are consistent with a reduction in solar modulation, providing a viable explanation for the exceptional GCR intensities in interplanetary space.

Keyword - Variation, GCR, solar wind, interplanetary, Cosmic Ray, Solar Cycle

-----X-----

INTRODUCTION

The heliosphere is beginning to resemble a gigantic asymmetric bubble filled of all kinds of energetic particles due to the superscopically increasing solar wind (SW). These particles, the main contributor to the space radiation environment, seriously jeopardize the health of astronauts and flight crew members in addition to the routine operation of high-altitude planes and satellites (e.g., Mertens & Slaba 2019). The three energetic particles that are usually observed in interplanetary space are solar energetic particles (SEPs), galactic cosmic rays (GCRs), and anomalous cosmic rays (ACRs).

Solar cosmic rays, or SEPs for short, are particles with energies ranging from a few tens of keV to several GeV that originate from the Sun. They are frequently connected to coronal mass ejections (CMEs) and solar flares. It is A CME-driven shock is an essential location for SEP acceleration (e.g., Hu et al. 2017, 2018; Fu et al. 2019; Ding et al. 2020). GCRs are generally regarded as stable backdrops, created by supernova blast shocks emitted by expanding supernova remnants (SNRs). This is confirmed by observations and numerical calculations (Aharonian et al. 2007, 2011; Ptuskin et al. 2010). There are some cosmic-ray species whose fluxes are significantly larger during

quiet times than background GCRs, or ACRs: H, He, C, N, O, Ne, and Ar (Hovestadt et al. 1973; McDonald et al. 1974; Hasebe et al. 1997). These species' initial ionization potentials are high. Conventional wisdom on ACRs states that they originate from from the interstellar medium; after being singly ionized by the solar wind or ultraviolet radiation, the neutral atoms drift into the heliosphere and are accelerated to energies above 10 MeV nuc⁻¹, primarily at or near the heliospheric termination shock (Mewaldt et al. 1993; Cummings & Stone 2007; Gloeckler et al. 2009). Giacalone et al. (2012) and the references therein are among the works that have put forth novel hypotheses for the acceleration of ACR. Zhao et al. (2019) suggested that reconnection processes in the heliosheath accelerate ACR protons. Comprehending the properties of energetic particles facilitates comprehension of the acceleration mechanisms and transport processes that occur between the sources and the observers.

When primary cosmic rays, or space-born GCR particles, strike Earth and puncture interacting with atmospheric atoms to create secondary particle cascades in the atmosphere of Earth (Mishev et al., 2014, for example). Since the majority of secondary particles are muons and neutrons at ground level,

ground-based muon detectors and neutron monitors (NMs) can measure the secondary particles once they reach the Earth's surface. The emergence of NMs dates back to the 1950s (Bieber 2013). The combination of GCR count rates from NM stations and GCR intensity from in situ satellites provides a reasonably complete picture of cosmic rays (CRs). Moreover, cosmogenic isotopes from tree rings and ice cores can aid in our understanding of GCRs over a longer time period (e.g., Owens & Forsyth 2013).

Propagation of cosmic radiation across the heliosphere significantly affected by the "solar modulation," or chaotic interplanetary magnetic field buried in the large-scale solar wind flow. Convection in the radially expanding solar wind, diffusion through the irregular interplanetary magnetic field (IMF), gradient and curvature drifts, and adiabatic deceleration (or adiabatic energy loss) are the four major modulation processes that are well described by the Parker transport equation (Parker 1965) (e.g., Sabbah 2000; Zhao & Zhang 2015; Ihongo & Wang 2016; Zhao et al. 2018). Secular data directly supports the assessment of their distinct contributions to cosmic-ray propagation during the last few decades (Kóta 2013).

Table 1: List of the Neutron Monitor Stations Used in this Work

NM Station	Abbrev.	Longitude (deg)	Latitude (deg)	Altitude (m)	P_c (GV)	E_0 (GeV)
Hermanns	HRMS	19.22	-34.42	26	4.58	12.67
Jungfraujoch	JUNG	7.98	46.55	3570	4.49	12.58
Newark	NEWK	-75.75	39.68	50	2.40	10.99
Oulu	OULU	25.47	65.05	15	0.81	10.30
Thule	THUL	-68.7	76.5	26	0.30	10.17

Note. P_c is the NM's local geomagnetic cut-off rigidity, and E_0 is the median energy of each NM station and is defined as: $E_0 = 0.0877 P_c^{1.154}$ (Jämsén et al. 2007; Usoskin et al. 2008).

Nevertheless, the numerical computation of cosmic-ray transit continues to be a very challenging task. The solar magnetic polarity, typically denoted as $[qA]$, where $[q]$ denotes a positively charged particle, is necessary to modulate cosmic-ray intensity. Positively charged particles typically drift inward along the heliospheric current sheet (HCS) when the heliospheric magnetic field at the north pole points inward (negative polarity, $qA < 0$), and outward along the HCS when the heliospheric magnetic field at the north pole points outward (positive polarity, $qA > 0$) (e.g., Jokipii & Thomas 1981; Belov 2000; Thomas et al. 2014). The 22-year heliomagnetic cycle, commonly referred to as the Hale cycle, alternates between a sharp (negative polarity, $qA < 0$) and flat-topped (positive polarity, $qA > 0$) shape. the cosmic ray intensity (McDonald et al. 2010)

In late 2009, both the GCR intensities from near-Earth spacecraft and the GCR count rates from ground-based NM stations reached their then all-time maximum levels (e.g., McDonald et al. 2010; Leske et al. 2013). Several features of the heliospheric environment during that time were unusual, including a prolonged solar minimum, a drop in the solar wind's

dynamic pressure, and a reduction in the interplanetary magnetic field and turbulence level (Mewaldt et al. 2010). The 2009 solar minimum features bigger particle mean free paths (MFPs) than previous solar minima due to the lower IMF turbulence, while particle drift velocities are higher due to the reduced magnitude of the IMF. These unusual interstellar activities would decrease the contribute to the unexpectedly high GCR intensities in 2009. Solar cycle 24 was the smallest magnitude in the space period, according to Hajra 2021. Along with these odd symptoms, it also displayed unusually flattened HCS, a drop in CME occurrences (Wang & Colaninno, 2014), and a decrease in sunspots, especially large ones (Chapman et al., 2014). It appears that there is grand minimum solar activity (Jiang & Cao 2018; Upton & Hathaway 2018; Gonçalves et al. 2020). According to earlier studies (e.g., Strauss & Potgieter 2014; Kuznetsov et al. 2017; Fu et al. 2020), the solar minimum P24/25 (also known as solar minimum P24/25) would see a GCR intensity peak that is either higher than or comparable to the level seen in 2009–2010. We will reexamine the GCR fluctuations across solar cycles 23 and 24, paying particular emphasis to the highest GCR intensities observed at 1 au during the solar minimum P24/25 timeframe. The paper is organized as follows. Section 2 lists the sources of the data set that was used in this study. The GCR observational results are presented in Section 3, which also looks into possible reasons for the extraordinary GCR intensities observed at 1 au in 2019–2020. Section 4 summarizes our work. The main source of inspiration for this essay

DATA DESCRIPTION

Since they don't add to the intensities that the Advanced Composition Explorer (ACE)/Cosmic Ray Isotope Spectrometer (CRIS) records, SEPs and ACRs are not included in the subsequent analysis.

The five NM stations listed in Table 1 monitor ground-level GCR count rates, while NASA's ACE spacecraft's in situ CRIS sensor detects GCR intensity at 1 au.

At the Sun-Earth L1 Lagrange point, the ACE spacecraft was launched on August 25, 1997, and has been continually monitoring solar wind plasma, interplanetary magnetic fields, and energetic particles (such as cosmic rays and SEPs) for over 24 years, spanning solar cycles 23 and 24 (Stone et al. 1998). The CRIS device was designed to measure the GCR intensities of 24 heavy species (with energies between 50 and 500 MeV nuc^{-1}), ranging from boron to nickel. The high atomic number and energy nuclei, in spite of their modest abundance ($\sim 1\%$), are particularly significant for space radiation as they contain a wealth of information on the cosmic rays' origin (e.g., Zhao & Qin 2013; Fu et al. 2020). The CRIS instrument captures the most comprehensive and statistically significant GCR data

to date, because to its huge geometric acceptance and excellent charge and mass resolution (Stone et al. 1998). The ACE Science Center (ASC) provides well-documented historical ACE/CRIS observations that are publically available at <http://www.srl.caltech.edu/ACE/ASC/index.html>. We utilize the reassessed level-2 CRIS products in this instance, and the data are arranged into 27-day Bartels rotation averages covering the period from August 26, 1997, to the present till October 31, 2020.

The pressure-corrected and 27-day averaged GCR count rates are computed using five NM stations: HRMS, JUNG, NEWK, OULU, and THUL. 1968 to 2020 are the years covered by these data. Table 1 offers comprehensive data regarding the five NM stations. The characteristic energy, or median energy, of EM is defined so that half of the detectors' counting rate is contributed by cosmic rays with energies greater (or lower) than EM (Usoskin et al. 2008; Zhao & Zhang 2016). Pc stands for each NM station's local geomagnetic cut-off rigidity. All data is derived from the Neutron Monitor Data Base.

The monthly mean sunspot number (SSN) can be obtained from the Solar Influences Data Analysis Center. The pressure differential of SW (Pd), the IMF magnitude (B) and the root mean square

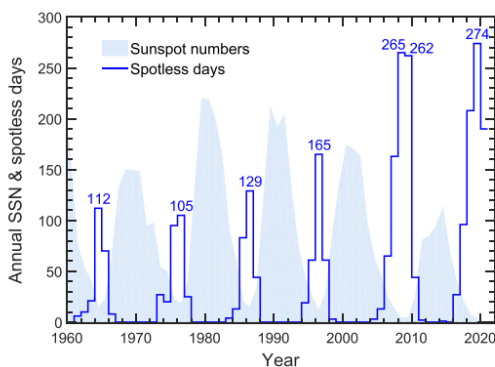


Figure 1. Yearly averaged sunspot numbers (shaded) and annual spotless days (histogram), up to 2020 October 31

The OMNIWeb database is used to get variations in the vector IMF (B). The Wilcox Solar Observatory database is used to calculate the HCS tilt angle and the mean solar polar magnetic field strength. The mean polar field is defined as $(N + S)/2$, where N is the strength of the polar field at the northern pole and S is the strength of the polar field at the southern pole. The halo CME lists are compiled from the SOHO/LASCO HALO CME catalog, and the yearly CME rates are compiled from the CACTus CME catalog (<http://www.sidc.be/cactus/>). Furthermore, the Cosmic Ray Telescope for the Effects of Radiation (CRaTER) sensor on board the Lunar Prospector measures the GCR radiation dose rates near the lunar surface. Accessible at Lunar Reconnaissance Orbiter (LRO)

Please take note that all of the aforementioned statistics are processed as a 27-day average unless otherwise specified.

RESULTS AND DISCUSSIONS

SSN measurements show that solar activity has been steadily falling since the early 1980s. The highest smoothed SSNs of solar cycles 21 through 24 are 232.9, 212.5, 180.3, and 116.4, respectively, as illustrated in Figures 1 and 2(a), indicating a significant drop in solar cycle amplitude. GCR movement in the heliosphere is affected by changes in solar activity. Intense solar activity (such as a CME or solar flare) can cause a cascade of space weather effects and effectively prevent GCR particles from entering the solar system (strong solar modulation), whereas a quiet Sun allows for increased GCR fluxes due to the lower modulation level. Following that, we examine the fluctuations in solar wind and interplanetary parameters caused by solar cycles. Section 3.1 summarizes the findings from GCR observations, including ground-level GCR counts and interplanetary GCR intensities; Section 3.2 presents the results of GCR observations; Section 3.3 looks at the impact of the inner heliospheric environment on GCR intensity, highlighting record-breaking fluxes during the solar minimum P24/25; Section 3.4 draws attention to a sharp drop in GCR intensity during the solar cycle 24's descending phase and offers a brief explanation of its possible causes; Section 3.5 shows the measured Galactic cosmic radiation doses on the lunar surface.

A Glance at Solar Cycles 20–24

Sunspots were first observed using a telescope in the early 1600s, and routine daily monitoring at the Zurich Observatory started in 1849. The number of sunspots fluctuates over time and exhibits an amazing quasi-11-year cycle, which is now widely accepted as a proxy for solar activity. Figure 1 illustrates that the maximum amplitude of the solar cycle has been decreasing since solar cycle 21, with the just completed solar cycle 24 being the lowest in human space travel history (Hajra 2021). Furthermore, 2019 has 274 days with no sunspots, the most in the past 107 years (since 1914). The extraordinary tranquil solar minimum permits us to look thoroughly into other big minima eras, such as the Maunder Minimum (1645-1715) and the Dalton Minimum (1790-1830).

Figure 2 depicts solar wind/interplanetary parameter changes in panels (b)-(f), as well as measured NM count rates in panel (g). These panels depict various well-known heliosphere and GCR features. (1) Both

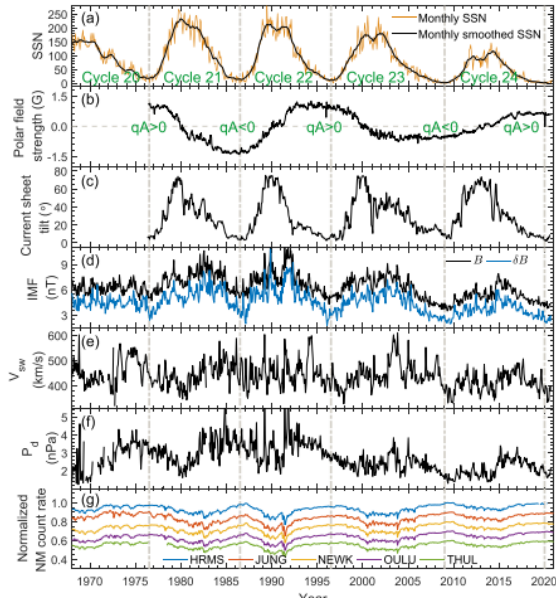


Figure 2 shows the 27-day average solar wind/interplanetary characteristics from January 1, 1968 to October 31, 2020. (a) The number of sunspots. (b) The average strength of the solar polar field. HCS Tilt angle (c). (d) The magnitude B of the IMF and its root mean square B. (e) The speed of the solar wind Vsw. Pd denotes the dynamic pressure of the solar wind. (g) Pressure-corrected NM count rates (normalized to P23/24 and multiplied by arbitrary variables to identify distinct stations). In panel (b), the magnetic field polarity depicted corresponds to that near the northern pole. The vertical dashed line marks the solar minimum period.

(2) GCR count rates at SSN are positively linked with the HCS tilt angle, IMF strength B, and turbulence B (i.e., the root mean square of the vector IMF);

SSN is inversely linked to ground level; (3) Every 11 years, the solar magnetic field switches polarity, corresponding to the 22-year heliomagnetic cycle (or Hale cycle); (4) the alternative (negative polarity, qA) peaked

Galactic Cosmic Rays During the 24th Solar Cycle

Low solar activity is projected to increase the number of GCR particles that enter the inner heliosphere and reduce the intensity of GCR modulation. Secular GCR data will be useful in highlighting the unique heliospheric conditions that occurred during the comparatively calm solar minimum P24/25. When compared to ground-based NM count rates, space-based GCR observations are short-lived and generally irregular, but those early cosmicray records (before to the launch of the ACE spacecraft) in interplanetary space may be replicated with a few more satellites or with a few more satellites.the application of cutting-edge numerical models such as the CRME model and the Badhwar-O'Neill model (Tylka et al., 1997).

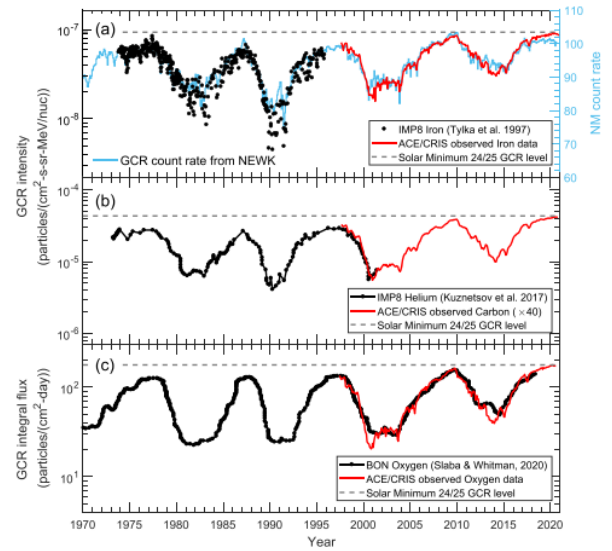


Figure 3. Secular variations of GCR intensities in interplanetary space and in NM count rates. (a) GCR iron intensities from ACE/CRIS at 129.1–428.7 MeV nuc1 (red curve) and from IMP-8 at 97.1-432 MeV nuc1 (black dots, taken from Tylka et al. 1997), using Newark GCR count rates (cyan curve, right axis) as a comparison. (b) ACE/CRIS GCR carbon intensities at 184.8-200.4 MeV nuc1 (red curve), compared to IMP-8/MED GCR helium intensities at 265 MeV nuc1 (black curve, based from Kuznetsov et al. 2017). (c) ACE/CRIS measured 69.4-237.9 MeV nuc1 integral oxygen fluxes (red curve) were compared to BON2020 predicted fluxes (black curve, based from Slaba & Whitman 2020). The horizontal dashed line represents the maximum GCR strength during the solar minimum P24/25.

GCR intensity profiles from 1970 to 2020, with ACE/CRIS iron intensities compared to IMP-8 in panel (a), and ACE/CRIS carbon intensities compared to helium in panel (b). IMP-8 intensities in panel (b), and ACE/CRIS oxygen intensities compared to BON2020 simulations in panel (c). Figure 3(a) also shows the GCR count rates from the NEWK station as a baseline. The peak value of GCR intensities at 1 au was previously reported to be the highest in the space age (McDonald et al. 2010; Mewaldt et al. 2010; Lave et al. 2013; Leske et al. 2013), but it is clear that maximum GCR intensities reach new heights during the solar minimum P24/25, as shown by Figure 3. The recent abnormally high GCR intensities at 1 au are essentially a result of unprecedented changes in the heliosphere, which will be discussed in further detail in Section 3.3. The average 27-day ACE/CRIS GCR intensity for solar cycles 23 and 24 is shown in Figures 4(a)-(c). Panel (a) shows the GCR intensities of the element oxygen at seven energy bins, panel (b) shows the intensities of twelve different species (C, O, Ne, Mg, Si, S, Ar, Ca, Ti, Cr, Fe, and Ni), and panel (c) shows the averaged intensities. For comparison, all profiles are

set to the solar minimum P23/24. The GCR intensities at 1 au in late 2009 are clearly stronger than those in early 2009, while slightly lower than those during the P24/25 solar minimum. GCR intensities are 25% higher in the solar minimum P24/25 than in the solar minimum P22/23, and 6% higher in the solar minimum P24/25. 24/P23.

The average 27-day NM count rates from 1997 to 2020 are shown in Figure 4(d). According to Moraal and Stoker (2010), NM count rates peak in late 2009, much like GCR intensity profiles do.

indicating that there is a higher chance of both high-energy (many GeV) and low-energy (1 GeV) GCR particles reaching Earth during the solar minimum P23/24 (Mewaldt et al. 2010). The greatest value of NM count rates in 2019–2020, however, falls short of the 2009 peak. is not compatible with interplanetary GCR intensities that have been measured. Ground-based NM stations only detect high-energy GCRS (several GeV) because of shielding effects of Earth's magnetosphere and atmosphere, however the ACE/CRIS instrument monitors relatively low-energy particles (1 GeV). The median energies (EM) of the five chosen NMs range from 10.17–12.67 GeV, which results in geomagnetic cut-off rigidities between 0.30 and 4.58 GV. The distinct ways that GCRS respond to changing solar activity both on Earth and in space might be explained by the differential modulation mechanisms. Figures

normalized value of 1, and the intensities are normalized to their solar minimum P23/24 values. CMEs are responsible for the pink-arrow decrease in the GCR intensity (see Section 3.4 for details).as particles with different energies pass through the heliosphere. We infer that low-energy GCR particles are more likely than high-energy particles to be affected by the decreased solar modulation during the solar minimum P24/25. Moreover, various variations in Earth's environmental fluctuations, including temperature, atmospheric water vapor, dynamic magnetospheric condition, atmospheric pressure, and snow influence, can have an impact on NM count rates (see Moraal & Stoker 2010, and references therein). We still don't know the exact cause of the difference in GCR strength on Earth and in interplanetary space.

Figure 4(e) shows the historical halo CMEs detected by LASCO on the SOHO mission since 1996. The conversation concerning this was shifted to Section 3.4 has a figure in it. energy spectra of the GCR elements C, N, O, and Fe, in that order; the spectral ratios of 2019-2009 and 2019-1997 are shown in Figures 5(c) and (d), respectively. At all lower and higher energies, there is a significant rise in GCR intensity during the solar minimum P24/25. GCR nuclei have different energy bands, although their intensity ratios are generally steady. The ratio for 2019-2009 falls between 1.20 and 1.30, whereas the ratio for 2019-1997 falls between 1.05 and 1.10. This is largely in line with the previous data, which shows that during the solar minimum P24/25, peak GCR intensities are 25% and 6% greater, respectively, than they were in late 1997 and early 1998.

2009, precisely. Additionally, the ratios at lower energies are somewhat greater than higher energies, suggesting that GCRs with lower energies are more vulnerable to changes in solar modulation than those with higher energies.

A comparison of the 27-day averaged GCR intensities for ACE/CRIS during solar cycles 23 and 24 is presented in Figure 6, where panel (a) represents 151.6-174.9 MeV nuc⁻¹ oxygen and panel (b) represents 170.8-232.9 MeV nuc⁻¹ iron. It is interesting to note that GCR intensities are significantly higher in solar cycle 24 than in cycle 23 throughout both ascending and falling stages. 10.17–12.67 GeV, which results in geomagnetic cut-off rigidities between 0.30 and 4.58 GV. The distinct ways that GCRS respond to changing solar activity both on Earth and in space might be explained by the differential modulation mechanisms. Figures 5(a) and (b) display the observed ACE/CRIS.

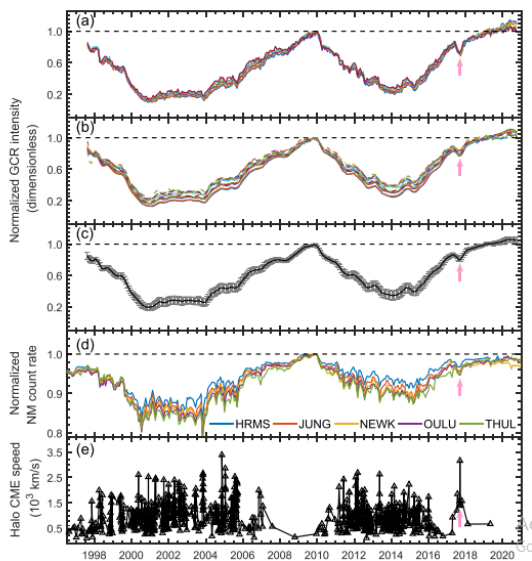


Figure 4(a) shows the oxygen element's ACE/CRIS GCR intensities at seven different energy intervals: 69.4–89.0 MeV nuc⁻¹, 91.0–122.5 MeV nuc⁻¹, 124.0–150.3 MeV nuc⁻¹, 151.6–174.9 MeV nuc⁻¹, 176.0–197.3 MeV nuc⁻¹, 198.3–218.0 MeV nuc⁻¹, and 219.1–237.9 MeV nuc⁻¹. (b) The twelve chosen GCR species' ACE/CRIS GCR intensities (C, O, Ne, Mg, Si, S, Ar, Ca, Ti, Cr, Fe, and Ni). (c) The twelve chosen GCR species' average intensities. (d) Rates of NM counts. (e) Halo CME occurrences in the past. The horizontal dashed line in panels (a) through (d) indicates the

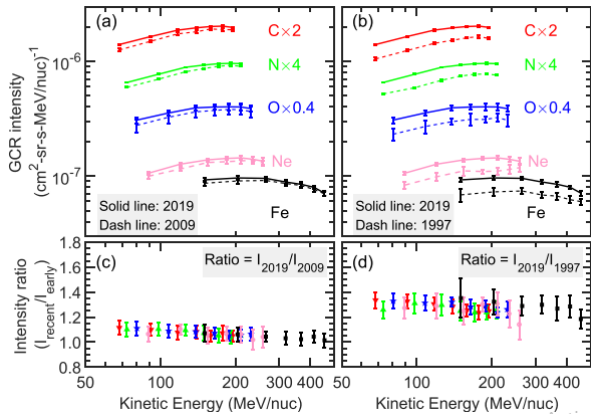


Figure 5. Panels (a) and (b) show the comparison of the ACE/CRIS GCR differential energy spectra between 2019 and 2009, and between 2019 and 1997, respectively. Energy spectra are multiplied by an arbitrary scale factor. Solid and dashed lines are quadratic fits to the experimental data. Panels (c) and (d) show the spectral ratios of the intensity between 2019 and 2009, and between 2019 and 1997, respectively.

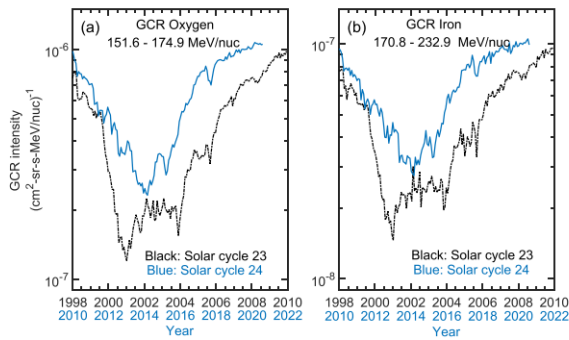


Figure 6. Comparison of 27 day averaged GCR intensities at 1 au between the solar cycles 23 (1998–2010) and 24 (2010–2020), for oxygen (a) and iron (b) expected result of a less active Sun and of weakened solar modulation in solar cycle 24. Furthermore, the bottom of the GCR profile in solar cycle 23 is deep and wide, but it is shallow and short-lasting in solar cycle 24. The former reflects a strong and continuous solar modulation, and the latter corresponds to a weakening and short duration solar modulation.

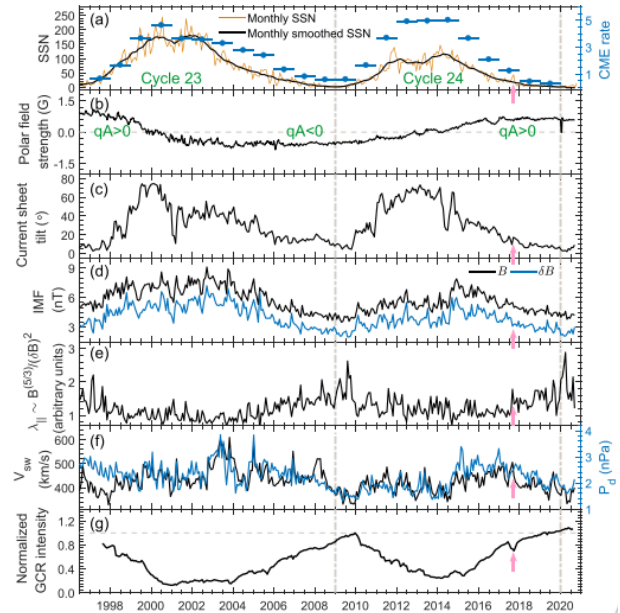


Figure 7. The 27 day averaged solar wind/interplanetary parameters from 1996 to 2020. (a) Sunspot number and annual CME rate. (b) Mean solar polar field strength. (c) HCS tilt angle. (d) IMF magnitude B and its root mean square δB . (e) Estimated parallel MFP λ_{\parallel} . (f) Solar wind speed (black curve) and dynamic pressure (cyan curve). (g) The 69.4–237.9 MeV nuc^{-1} GCR oxygen intensity from ACE/CRIS (normalized to the solar minimum P23/24), and the horizontal dashed line represents the normalized GCR intensity equal to 1. The pink-arrow dip in the GCR intensity was caused by CMEs (see Section 3.4 for details).

Inner Heliospheric Environment during Solar Cycle 24

The unprecedented GCR intensities at 1 au during the solar minimum P24/25 naturally raise the question of what factors are at work. The pace of CMEs, the intensity of the Sun's polar magnetic field, the tilt angle of HCS, the strength and turbulence of the interplanetary magnetic field, and the speed and dynamic pressure of the solar wind are all examples of broad answers.

Coronal Mass Ejection Rate

When CME-driven shocks or possibly attractive mists pass through, they generally transport more grounded attractive fields than the surrounding sun-based breeze and generate savage interplanetary disturbing affects and appealing protection of charged particles. As a result, massive CMEs successfully prevent massive beam particles from dispersing in the inner heliosphere (Wibberenz et al. 1998; Stick 2000; Kilpua et al. 2017). Furthermore, CMEs are frequently accompanied by other forms of sun-based activity, such as solar flares (Vrnak 2016; Syed Ibrahim et al. 2018), eruptive prominences,

and X-beam sigmoids (Gibson et al. 2002; Pevtsov 2002), which increase GCR particle protection.

Figure 7(a) depicts the annual rate of CMEs obtained from the automated Cactus list between 1997 and 2019. It demonstrates that the speed of CMEs in 2019 is 0.29, which is 56% and 52% lower than in 1997 and 2009, respectively. The smaller quantity of CMEs causes fewer appealing irregularities to control GCR dispersion, which contributes to an increase in GCR mobility. Despite the low quantity, Wang and Colaninno (2014) argued that the speed and mass of CMEs in solar cycle 24 are much lower than those in solar cycle 23. These intriguing, slow-moving, and less massive CMEs impede the sunlight-based correction of astronomy beams. 2013 (Paouris)

Solar Polar Field

Every 11 years, the extreme of the Sun's polar fields reverses or flips over (Babcock and Livingston 1958; Babcock 1959; Owens and Forsyth 2013). The latest two inversions happened in 2001 and 2014, respectively, and it is now in the positive extreme ($q_A > 0$). The Sun's polar fields also exhibit unusual properties in the new two cycles, for example, the noticeably debilitated polar attractive fields in sun powered cycle 24 (Sun et al. 2015; Mordvinov et al. 2016; Janardhan et al. 2018).

The Sun's polar fields influence GCR entry into the heliosphere by modifying the sun-based wind stream design and the magnitude of the IMF (Lee et al. 2009). It is taken into account that the Sun's polar field strength in sun oriented cycle 23 is 50% lower than that in cycles 21-22, and the transition of the open attractive field line at the World's circle begins to be the most decreased about 1963 (Ahluwalia and Ygbuhay 2010). As shown in Figures 2(b) and 7(b), the solar's polar field strength begins to recover after 2014 and enters a level period after the year 2017 with a stable strength of 0.6 G, which is unusually close to or marginally greater than that in solar powered cycle 23. It is possible that additional GCR will be released. As a result of the sun's devastating polar field, particles enter the heliosphere.

Tilt Angle of the Heliospheric Current Sheet

Previous studies focused on the GCR force because of a wavy interplanetary current sheet, and discovered a reverse link between the HCS slant point and the GCR power (Jokipii and Thomas 1981; Potgieter et al. 2001). It is on the grounds that the GCR particles essentially float outward ($q_A > 0$ extremity) or internal ($q_A < 0$ extremity) along the HCS close to the sun powered equator, and an enormous slant point implies that the vast beam particles need to float a more drawn out way length toward the Earth, prompting an expansion in the delay between the source and the eyewitness (Ferreira and Potgieter 2004; Mewaldt et al. 2010; Zhao et al. 2014; Ross and Chaplin 2019). The HCS slant point's variation might have considerable, if not dominant, effects on the GCR

adjustment process during the sun-based minimum age. Similarly, when $q_A > 0$, the float of GCRs along the HCS has a larger role than the dissemination.

Figure 7(c) depicts the global variation of the HCS slant point. The slant point begins to decline after 2014, reaching a low point of 2.1° in 2020 April, which is 22% lower than the sun powered least P22/23 and 53% lower than the sun orientated least P23/24. This exceptionally low slant point reflects an unusually near arrangement to the sun-powered core HCS, resulting in an improved outward float speed (for $q_A > 0$) and greatly increased GCR power. As seen in Figure 7(g), the HCS slant point begins to rise in 2020 May and reaches a value of 14.8° by the end of 2020 November, accompanied by the steady fall of the GCR motion.

IMF Strength and Turbulence Level

The interplanetary magnetic field influences both drifts and cosmic-ray diffusion, and cosmic-ray intensities are demonstrated to be inversely related to IMF strength (denoted by B). As B lowers, GCR drift velocity increases (e.g., Jokipii & Levy 1977; Jokipii & Kota 1989). Turbulence in the IMF, on the other hand, influences cosmic ray pitch-angle scattering, where the diffusion coefficient is proportional to $1/B$ or a power of $1/B$ (e.g., Jokipii & Davila 1981; Ferreira & Potgieter 2004). The turbulent IMF's cosmic-ray diffusion has both parallel and perpendicular components, and the connection between the diffusion coefficient (λ) and the mean free path (λ) of a particle is given by:

$$\lambda_{\perp, \parallel} \equiv 3\kappa_{\perp, \parallel}/v,$$

λ_{\perp} and λ_{\parallel} signify parallel and perpendicular MFPs, respectively, while κ_{\perp} and κ_{\parallel} denote parallel and perpendicular diffusion coefficients (Zank et al. 1998; Pei et al. 2010). The radial MFP λ_r , which is dictated by the parallel diffusion λ_{\parallel} , is virtually constant inside the inner heliosphere (Zhao et al. 2017). Parallel MFP λ_{\parallel} is approximately three orders of magnitude smaller than perpendicular MFP λ_{\perp} (Zhao et al. 2018). The perpendicular diffusion λ_{\perp} is commonly thought to scale as the parallel diffusion λ_{\parallel} (Ferreira & Potgieter 2004).

The parallel MFP λ_{\parallel} is proportional to B^{-2} ($\lambda_{\parallel} \propto B^{-2}$), where B is the mean IMF magnitude and B_{rms} is the root mean square of the angular velocity. Vector fluctuation in the IMF (Zank et al. 1998; Mewaldt et al. 2010). Using the simplified relation $\lambda_{\parallel} \propto B^{-2}$ ($\lambda_{\parallel} \propto B^{-2}$), the parallel MFP component λ_{\parallel} at 1 au is determined spanning cycles 23 and 24. In the solar minimum P24/25, the IMF magnitude B reaches a minimum of 3.8 nT, which is 24% lower than the solar minimum of cycles 20-22 (5 nT), but 5.6% higher than the minimum in late 2009 (3.6 nT). The IMF turbulence B is 2.1 nT at the solar minimum P24/25, which is 5% higher than at the solar minimum P23/24. Because of the weak IMF and turbulence, the estimated

cosmic-ray MFP (P) rises substantially, as does the maximum value. The letter P in the P24/25, the solar minimum, is 31% greater than in 1997 and 10% higher than in 2009. The prominent peak on the P profile (about 2020 March) is followed by unparalleled GCR intensity.

Solar Wind The solar wind

The status of the heliosphere (including speed, density, and temperature) changes throughout time and influences GCR movement. In general, a low solar wind speed reduces both the outward convective rate of GCRs and the adiabatic energy loss rate. GCR intensities have been found to be anticorrelated with solar wind speed, implying that the lower the solar wind, the higher the GCR intensities, and vice versa (e.g., Zhao et al. 2014; Ihongo & Wang 2016).

Figure 7(f) depicts the temporal change of the SW speed (V_{sw} , black curve) and the SW dynamic pressure (P_d , blue curve). The last three solar minimum eras' average speed was 371.19 km/h.

A Sudden Dip in the GCR Intensity during the Descending Phase of Cycle 24

During the falling phase of solar cycle 24, the GCR intensity at 1 au decreases for a brief but significant period in the second half of 2017 (around September), after which it resumes its upward trend. This dip is also recorded by ground-based NM stations, as illustrated by the pink arrows in Figures 4 and 7.

This GCR anomaly is most likely produced by solar wind and interplanetary disturbances. Between September 4 and September 10, 2017, a series of CMEs (including the fastest halo CME on September 10, see Figure 4(e)) impacted the interplanetary and geospace environment (Guo et al. 2018; Lee et al. 2018; Ding et al. 2020). Furthermore, the growing number of sunspots (Figure 7(a)) and the increased HCS. Because of the increased solar modulation, the higher SW speed (Figure 7(f)) and tilt angle (Figure 7(c)) may result in a drop in GCR intensity.

Dose Rate of GCR Radiation on the Moon's Surface Deep-space radiation, which includes both solar particles and GCRs, is a major threat to manned space missions. As a result, the long-term and short-term radiation effects must be considered while designing a deep-space expedition. As a constant background of energetic particles, GCRs are the most hardest to fight against, and they can pose major threats to people and precise payloads aboard spacecraft. Previously, Schwadron et al. (2010) discovered that the GCR dose rates near the lunar surface are the greatest during the extended solar minimum P23/24. The recording process began. This is the year 1987. We are naturally intrigued about the current space radiation environment, given that the peak value of GCR intensities in the solar minimum P24/25 is significantly greater than that in the 2009

solar minimum. The LRO's Cosmic Ray Telescope for the Effects of Radiation (CRaTER) instrument was developed to research the lunar radiation environment and is presently 50 kilometers away from the Moon (Spence et al. 2010). Since its launch on June 18, 2009, the LRO has been exploring the lunar radiation environment. Figure 8 displays the hourly and daily average dosage rates of the LRO/CRaTER, with the horizontal dashed-dotted line reflecting the maximal value of dose rates. The solar minimum is P24/25. It is possible. demonstrated a high correlation between the dosage rates and the intensity of the GCR and solar activity. During the recent solar minimum, the GCR radiation dose rate and intensity rose dramatically due to the declining solar modulation. We find that the first half of 2020 will see a 5% increase in dose rates at their peak value compared to 2009–2010, which corresponds to a 6% increase in GCR intensities measured at 1 au. The stakes for radiation shielding and protection in space have increased since, in our opinion, this is the greatest dose rate on the lunar surface since the 1980s. Our research provides a point of reference for the development of spacecraft materials for future deep-space travel, as well as the ability to predict the risk that GCR space radiation poses to individuals in near-Earth orbit. airplanes.

CONCLUSIONS

The Sun was extraordinarily tranquil during the recently concluded solar cycle 24, with very low sunspot numbers, an exceptionally flat HCS, a decreased CME eruption rate, and a weak interplanetary magnetic field and turbulence level. GCR intensities observed in interplanetary space (as well as on Earth) are sensitive to heliospheric conditions, a process known as solar modulation. We focus on the oscillations in GCR intensity from 1997 to 2020 using ACE/CRIS measurements, and we investigate the influence of inner heliospheric conditions on GCR intensities. The long-term changes of ground-based NM count rates are also addressed. The results are summarized below.

1. GCR intensities observed at 1 au exceed the highest values in the solar minimum P24/25 since the deployment of the ACE satellite, which is P22/23 is 25% greater than the solar minimum, while P23/24 is 6% higher. With the combination of IMP-8 data and BON2020 numerical modeling results, we reveal that GCR intensities were at their highest since the beginning of the space era during the present solar minimum, with particle energy ranging from tens to hundreds of MeV nuc^{-1} . According to LRO/CRaTER data, the record-breaking GCR intensity at 1 au increase radiation dose rates near the lunar surface by 5% over the solar minimum P23/24.

2. The highest NM count rate at P24/25 is lower than it was in late 2009. The difference in GCR intensity in interplanetary space and NM count rates appears to be caused by modulation mechanisms. both high- and low-energy particles. We think that high-energy

GCR particles are modulated less than low-energy GCR particles, meaning that low-energy GCR particles are more susceptible to fluctuating solar modulation. Another idea holds that NM count rates are affected by conditions in the Earth's magnetosphere and atmosphere. It will be investigated further in a subsequent study.

3. We discover that the mean solar polar field strength remains moderate during the solar minimum P24/25, similar to the value seen during the 2009 solar minimum; the HCS tilt angle hits a minimum of 2.1° in 2020 April, 22% less than in the solar minimum P22/23 and 53% less than in the solar minimum P23/24; the CME The estimated cosmic-ray MFP (λ_P) has increased by around 10% since late 2009 because to the relatively low strength and turbulence of the IMF. The eruption rate is quite tiny, less than half of the CME rate during the solar minima P22/23 and P23/24. Together, these factors result in decreased solar modulation and a remarkable increase in GCR intensity.

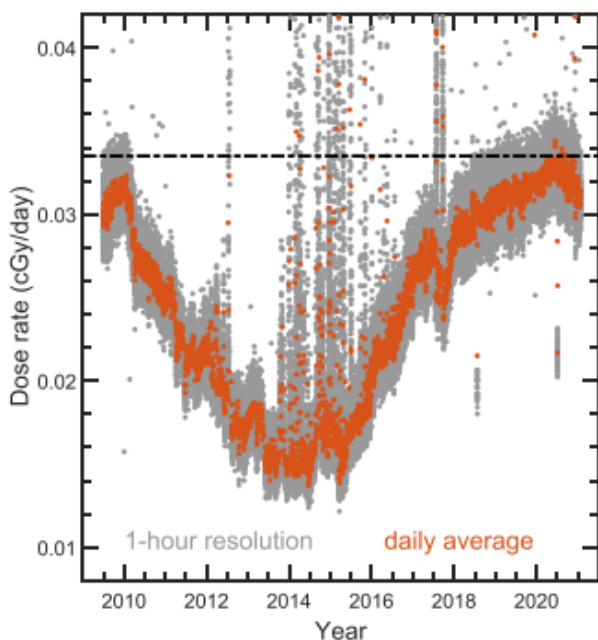


Figure 8. GCR radiation dose rates on the lunar surface measured by the LRO/ CRaTER. The horizontal dashed-dotted line marks the peak value of dose rate in the solar minimum P24/25.

This study is mainly statistical in nature, examining GCR changes in the extremely low energy range (50-500 MeV nuc^{-1}). We investigate the unusual heliospheric conditions in the inner heliosphere to explain our findings of record-breaking GCR strength at 1 au. It is vital to explore the extent to which heliospheric fluctuations influence GCR intensity. Numerical models of the effects of drifts, diffusion, and convection on cosmic-ray modulation are being developed (e.g., Strauss & Potgieter 2014; Zhao et al. 2014; Shen & Qin 2018; Shen et al. 2019).

REFERENCES

1. Aharonian, F., Akhperjanian, A. G., Bazer-Bachi, A. R., et al. 2007, *A&A*, 464, 235
2. Aharonian, F., Akhperjanian, A. G., Bazer-Bachi, A. R., et al. 2011, *A&A*, 531, C1
3. Ahluwalia, H. S., & Ygbuhay, R. C. 2010, in *AIP Conf. Proc.* 1216, 12th Int. Solar Wind Conf., ed. M. Maksimovic et al. (Melville, NY: AIP), 699
4. Babcock, H. D., & Livingston, W. C. 1958, *Sci*, 127, 1058
5. Bieber, J. W. 2013, in *AIP Conf. Proc.* 1516, Centenary Symp. 2012: Discovery of Cosmic Rays, ed.
6. J. F. Ormes (Melville, NY: AIP), 234 Cane, H. V. 2000, *SSRv*, 93, 55
7. Chapman, G. A., de Toma, G., & Cookson, A. M. 2014, *SoPh*, 289, 3961
8. Cummings, A. C., & Stone, E. C. 2007, *SSRv*, 130, 389
9. Ding, Z. Y., Li, G., Hu, J. X., et al. 2020, *RAA*, 20, 145
10. Ferreira, S. E. S., & Potgieter, M. S. 2004, *ApJ*, 603, 744
11. Fu, S., Jiang, Y., Airapetian, V., et al. 2019, *ApJL*, 878, L36
12. Fu, S., Zhao, L., Zank, G. P., et al. 2020, *SCPMA*, 63, 219511
13. Giacalone, J., Drake, J. F., & Jokipii, J. R. 2012, *SSRv*, 173, 283
14. Gibson, S. E., Fletcher, L., Del Zanna, G., et al. 2002, *ApJ*, 574, 1021
15. Gloeckler, G., Fisk, L. A., Geiss, J., et al. 2009, *SSRv*, 143, 163
16. Gonçalves, Í. G., Echer, E., & Frigo, E. 2020, *AdSpR*, 65, 677
17. Guo, J., Dumbović, M., Wimmer-Schweingruber, R. F., et al. 2018, *SpWea*, 16, 1156
18. Hasebe, N., Kondoh, K., Mishima, Y., et al. 1997, *AdSpR*, 19, 813
19. Hovestadt, D., Vollmer, O., Gloeckler, G., et al. 1973, *PhRvL*, 31, 650
20. Hu, J., Li, G., Ao, X., et al. 2017, *JGRA*, 122, 1093
21. Hu, J., Li, G., Fu, S., et al. 2018, *ApJL*, 854, L1
22. Ihongo, G. D., & Wang, C. H. T. 2016, *Ap&SS*, 361, 44
23. Jämsén, T., Usoskin, I. G., Rähkä, T., et al. 2007, *AdSpR*, 40, 342
24. Janardhan, P., Fujiki, K., Ingale, M., et al. 2018, *A&A*, 618, A148
25. Jiang, J., & Cao, J. 2018, *JASTP*, 176, 34
26. Jokipii, J. R., & Davila, J. M. 1981, *ApJ*, 248, 1156
27. Jokipii, J. R., & Kota, J. 1989, *GeoRL*, 16, 1
28. Jokipii, J. R., & Levy, E. H. 1977, *ApJL*, 213, L85
29. Jokipii, J. R., & Thomas, B. 1981, *ApJ*, 243, 1115
30. Kilpua, E., Koskinen, H. E., & Pulkkinen, T. I. 2017, *LRSP*, 14, 5

31. Kuznetsov, N. V., Popova, H., & Panasyuk, M. I. 2017, JGRA, 122, 1463
32. Lave, K. A., Wiedenbeck, M. E., Binns, W. R., et al. 2013, ApJ, 770, 117
33. Lee, C. O., Jakosky, B. M., Luhmann, J. G., et al. 2018, GeoRL, 45, 8871
34. Lee, C. O., Luhmann, J. G., Zhao, X. P., et al. 2009, SoPh, 256, 345
35. Leske, R. A., Cummings, A. C., Mewaldt, R. A., et al. 2013, SSRv, 176, 253
36. McDonald, F. B., Teegarden, B. J., Trainor, J. H., et al. 1974, ApJL, 187, L105
37. McDonald, F. B., Webber, W. R., & Reames, D. V. 2010, GeoRL, 37, L18101
38. Mertens, C. J., & Slaba, T. C. 2019, SpWea, 17, 1650
39. Mewaldt, R. A., Cummings, A. C., Cummings, J. R., et al. 1993, GeoRL, 20, 2263
40. Mewaldt, R. A., Davis, A. J., Lave, K. A., et al. 2010, ApJL, 723, L1
41. Mishev, A. L., Kocharov, L. G., & Usoskin, I. G. 2014, JGRA, 119, 670
42. Moraal, H., & Stoker, P. H. 2010, JGRA, 115, A12109
43. Mordvinov, A., Pevtsov, A., Bertello, L., et al. 2016, STP, 2, 3 Owens, M. J., & Forsyth, R. J. 2013, LRSP, 10, 5
44. C., Bieber, J. W., Breech, B., et al. 2010, JGRA, 115, A03103 Pevtsov, A. A. 2002, SoPh, 207, 111
45. Potgieter, M. S., Burger, R. A., & Ferreira, S. E. S. 2001, SSRv, 97, 295
46. Ptuskin, V., Zirakashvili, V., & Seo, E.-S. 2010, ApJ, 718, 31
47. Schwadron, N. A., Boyd, A. J., Kozarev, K., et al. 2010, SpWea, 8, S00E04
48. Spence, H. E., Case, A. W., Golightly, M. J., et al. 2010, SSRv, 150, 243
49. Stone, E. C., Cohen, C. M. S., Cook, W. R., et al. 1998, SSRv, 86, 285
50. Strauss, R. D., & Potgieter, M. S. 2014, SoPh, 289, 3197
51. Sun, X., Hoeksema, J. T., Liu, Y., et al. 2015, ApJ, 798, 114
52. Syed Ibrahim, M., Shanmugaraju, A., Moon, Y. J., et al. 2018, AdSpR, 61, 540
53. Thomas, S. R., Owens, M. J., & Lockwood, M. 2014, SoPh, 289, 407
54. Tylka, A. J., Adams, J. H., Boberg, P. R., et al. 1997, ITNS, 44, 2150
55. Upton, L. A., & Hathaway, D. H. 2018, GeoRL, 45, 8091
56. Usoskin, I. G., Braun, I., Gladysheva, O. G., et al. 2008, JGRA, 113, A07102 Vršnak, B. 2016, AN, 337, 1002
57. Wang, Y. M., & Colaninno, R. 2014, ApJL, 784, L27
58. Wang, Y. M., Robbrecht, E., & Sheeley, N. R. 2009, ApJ, 707, 1372
59. Wibberenz, G., Le Roux, J. A., Potgieter, M. S., et al. 1998, SSRv, 83, 309
60. Zank, G. P., Matthaeus, W. H., Bieber, J. W., & Moraal, H. 1998, JGRA, 103, 2085
61. Zhao, L. L., Adhikari, L., Zank, G. P., et al. 2017, ApJ, 849, 88

Corresponding Author

Brijesh Dwivedi*

Phd Scholar, APSU Rewa